Extraction of Ocean Wave Directional Spectra Using Steerable Doppler Side-Scan Sonars

MARK V. TREVORROW

Ocean Physics, Institute of Ocean Sciences, Sidney, British Columbia, Canada

IAN J. BOOTH

Autonetics Research Associates, Sooke, British Columbia, Canada

(Manuscript received 13 March 1994, in final form 15 February 1995)

ABSTRACT

A new technique is presented for extraction of ocean wave directional spectra using steerable Doppler side-scan sonars. The method is designed for use from a subsurface platform at the 25-m depth. Two 360° steerable side-scan beams at 103 kHz are used to estimate along-beam horizontal water motion due to waves at ranges out to 250 m. Upward-looking sonars are used to estimate the surface height power spectrum. This new method, dubbed "coherent wavenumber summation," uses wavenumber decomposition of radial velocity versus range profiles. A wavenumber-directional grid is then coherently incremented over one 360°, 64-ping sweep of the side-scan beams, which requires deconvolution in time and spatial orientation. The resulting directional spreading functions are then incoherently averaged over 30–50 min of side-scan data. Numerical testing shows that this method can reconstruct accurately realistic uni- and bidirectional seas over the frequency range 0.09–0.30 Hz and is insensitive to random noise. The method is demonstrated through comparison with conventional array methods using data collected in the northeast Pacific. The resolution of this method is severely limited by the combined effects of short temporal and spatial coherence scales of natural ocean waves, and geometric consequences of the finite side-scan beam aperture (<200 m).

1. Introduction

Recently, exciting new techniques for probing ocean surface processes using underwater acoustics have emerged. These new techniques take advantage of the fact that copious quantities of microscopic air bubbles are injected at the ocean surface (Crawford and Farmer 1987; Farmer and Vagle 1989). This microbubble generation is strongly driven by breaking wave activity, which in turn is linked to ocean surface wind and wave dynamics. Due to their small size, large acoustic target strength, and large numbers, these microbubbles serve as excellent tracers of water particle motions. There is a readily measurable acoustic Doppler frequency shift in the side-scan echoes due to the large orbital velocities induced by surface waves. This horizontal Doppler velocity versus range has been previously used to investigate ocean surface waves (Krogstad et al. 1988; Pinkel and Smith 1987; Smith 1989; Herbers et al. 1991) and is the focus of this paper.

This work presents a new technique for the extraction of frequency-directional spectra of ocean surface waves using continuously rotating Doppler side-scan sonars. Recent work (Trevorrow 1995, hereafter referred to as T95) has demonstrated the use of *fixed orientation* side-scan arrays in measurement of directional spectra. Much of the discussion that is given in T95 regarding Doppler velocity measurement and platform motion corrections is directly applicable here (and will not be repeated). Two side-scan beams are used in an azimuthally sweeping mode, each covering a complete circle (counterrotating) every 76.8 s. With a rotating beam geometry it is not possible to perform time-frequency transforms, which form the basis for conventional processing schemes for array and buoy data. The entire frequency-directional spectrum must be solved simultaneously. The current approach uses wavenumber decomposition of the along-beam horizontal velocity profiles with range, which are coherently summed over one 360° side-scan sweep. Then the directional distributions at each wavenumber magnitude are incoherently averaged over roughly 40 min of wave data. Thus, this method has been dubbed "coherent wavenumber summation" (CWS). The coherent summation algorithm uses the wavenumber distortion induced by measuring waves along directions other than their propagation direction. The swept geometry has some merits, in addition to the Doppler velocity results, because useful two-dimensional images of microbubble spatial distributions can be derived simultaneously from the side-scan backscattered intensity (e.g., Trevorrow et al. 1994). Additionally, this method

Corresponding author address: Dr. Mark V. Trevorrow, Ocean Physics, Institute of Ocean Sciences, P.O. Box 6000, 9860 West Saanich Road, Sidney, BC V8L 4B2, Canada.

could be applicable to the similar problem of radar or lidar-based estimation of surface wave directional spectra.

2. Measurement of Doppler velocity

This work uses data from the SeaScan platform (see Trevorrow and Teichrob 1994 for a detailed description), which supports six upward-looking conical beam sonars (28–397 kHz) and two steerable side scans mounted on a platform that is either bottom moored or suspended from a surface float at 25–30-m depth. SeaScan uses two computer controlled, 360° steerable side scans transmitting at 103 kHz. A sketch of the sonar and side-scan geometry is shown in Fig. 1. The orientation of the platform relative to the earth is known from an onboard compass, and the orientation of each side-scan beam relative to the platform is known from internal angular sensors. The side-scans have fan beams, with horizontal beamwidth (to −3 dB) of ±1.5° and vertical beamwidth of ±25°. The main axis of the side scans is elevated 15° above horizontal. The side scans are each stepped through 360° (counterrotating) in 128 steps (2.813° resolution), with a ping–listen–step cycle duration of 0.6 s.

The echo received by the sonars and side scans will be the integration of microbubble, surface, and other particulate scattering distributed within the insonified volume. For wind speeds greater than roughly 5 m s^{-1}, however, there is sufficient white-capping activity to create a near-surface scattering layer of microbubbles. As discussed in T95, the side-scan echo (intensity and Doppler velocity) is dominated by *near-surface* (<3 m depth) microbubble distributions and wave velocities. The Doppler velocity measurement is *radial* velocity, confined in the horizontal plane to ±1.5° of the heading of the side-scan beam and with vertical grazing angle decreasing with increasing range. The larger grazing angles at short ranges create a problem by introducing vertical components of the wave velocity, which are 90° out of phase with the horizontal components and can be removed only by frequency separation. This problem can be partially alleviated by using data from horizontal ranges of greater than 50 m, so that the grazing angle is less than approximately 25°. Note that the side-scan echo decays roughly as (range)$^{-2}$, so that larger ranges will encounter signal-to-noise problems. In practice ranges of up to 250 m can be successfully scanned with the current instrumentation (which is still under development), and it should be possible to improve on this range limitation in the future. As discussed in T95, attention must be paid to motions of the platform, which are generally coupled to the wave orbital motion at low frequencies (~0.08 Hz). Range averaging of the horizontal Doppler velocity (corrected for grazing angle) along a side-scan beam can be used to estimate the platform motion and also yields a component of the surface drift current relative to the instrument platform. From one 360° sweep the mean magnitude and direction of this surface current can be calculated from the first circular harmonic of this azimuthal velocity. This can then be vectorally time averaged.

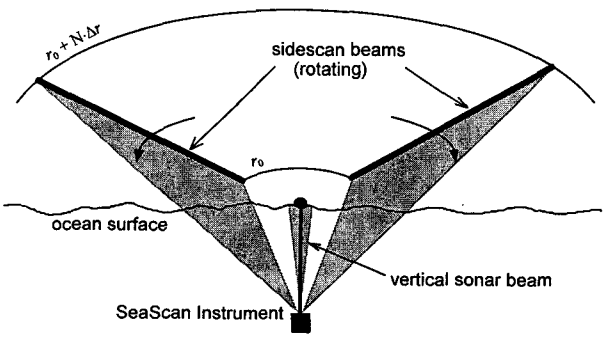

FIG. 1. Sketch of rotating side-scan geometry from the SeaScan acoustics platform. Platform is suspended at 25-m (nominal) depth, with side-scan maximum range of 280 m.

A 4.35-ms phase-encoded pulse is transmitted simultaneously by the two 103-kHz side scans. The side-scan echo is collected for 390 ms, allowing a maximum horizontal range of about 289 m. The Doppler shift (and thus velocity) of the signal is calculated using standard time-domain complex covariance algorithms. Recent work (Pinkel and Smith 1992; Brumley et al. 1991; Trevorrow and Farmer 1992) investigated coded pulses in this context as a means to reduce Doppler velocity variance. SeaScan uses 4.6 repetitions of a 7-bit Barker code (32 bits total), with a bit length of 0.1361 ms, yielding a range resolution of 3.2 m. For this side-scan pulse setup, the velocity uncertainty (square root of variance) is 0.14 m s^{-1}, and the Doppler velocity aliasing limit occurs at ±3.8 m s^{-1}. As discussed in T95, natural bubble cloud spatial and temporal variability increases the *effective* velocity estimation noise level to approximately 0.2 m s^{-1}.

The sea surface elevation is also routinely calculated as part of the sonar processing, as described in T95 and by Zedel (1994). The six vertical sonars fire a short (0.5 ms) ping that is used for volume scattering and surface elevation measurements. The surface heights from the three highest frequency sonars (with the narrowest beams) are averaged together to yield an estimate with resolution ±0.03 m. The height spectrum is then calculated using standard FFT (fast Fourier transform) spectral analysis from (nominally) 40 to 50 min of sonar derived surface heights. A vertical accelerometer signal, double integrated and high-pass filtered at 0.04 Hz, is used to subtract the vertical displacement of the instrument platform.

3. Extraction of directional spectrum

The directional spectrum of ocean surface gravity waves describes the frequency and azimuthal distri-

bution of wave height power and is denoted here as $G(f, \theta)$, where f is the frequency (Hz) and θ the azimuthal angle (radians or degrees) that the waves propagate toward. All computations are done with angles defined in the mathematical sense and then converted to compass headings (clockwise from north) for display. Conceptually, we can divide the directional spectrum into two constituents,

$$G(f, \theta) = D(f, \theta)S(f), \quad (1)$$

where $D(f, \theta)$ is the directional spreading function, containing information on the spread of wave energy at each frequency, and $S(f)$ is the one-dimensional wave height spectrum, containing information on the total wave power at each frequency. The decomposition in Eq. (1) requires that the directional spreading functions at each frequency be normalized according to

$$\int_0^{2\pi} D(f, \theta)d\theta = 1. \quad (2)$$

This separation is convenient as we need only focus on calculation of $D(f, \theta)$. Here $S(f)$ can be calculated accurately from the surface elevation data collected with the vertical sonars. This also implies that absolute amplitude information need not be carried through the calculation of $D(f, \theta)$, because it will be normalized.

In all of the following analysis we shall assume deep-water linear water wave dispersion and particle motion, but this method could be adapted to shallow-water or nonlinear descriptions. The familiar dispersion relation between angular frequency ω ($=2\pi f$) and wavenumber k ($=2\pi/\lambda$, where λ is the wavelength) is

$$\omega^2 = gk \quad \text{or} \quad \lambda = \frac{g}{2\pi f^2}, \quad (3)$$

where g is the acceleration due to gravity (9.805 m s^{-2}). We shall also use an assumption that the microbubble scatterers lie at or near the surface, which was examined in T95.

For this CWS method, we are constrained to the frequency range 0.08–0.30 Hz. Under typical ocean conditions the wave velocity power spectrum has a peak near 0.1 to 0.2 Hz and decreases with frequency as f^{-3} above this spectral peak. This decreasing wave velocity relative to the side-scan *estimation noise* level (typically about 0.2 m s^{-1}) limits measurements at higher frequencies. As shown in the T95, natural bubble clouds exhibit 0.5–1.5-m e-folding depth scales and considerable spatial and temporal variability, which results in degraded wave velocity measurements at frequencies greater than 0.3 Hz and ranges greater than 150 m. The lower frequency limit corresponds to a wavelength of 244 m, which is constrained by the maximum range aperture of the side-scan beam.

Each of the two side-scans on the SeaScan platform covers a 180° arc in a sequence of 64 pings (2.813° steps), which at 0.6 s per ping takes 38.4 s. The two side scans are counterrotating, with each covering an opposite semicircle during a 64-ping sequence. This sequence is continuously repeated for periods of 60 min or more. At each ping the side-scans measure (nearly) horizontal water velocity, using microbubbles as tracers, at equally spaced range intervals along a radial line extending from 20- to nearly 295-m range. The velocity measured is the (nearly) horizontal component parallel to the measurement direction. This current approach will make use of the spatial-to-wavenumber transform of horizontal velocity along each side-scan beam as it is swept through a full circle.

For discussion purposes, consider a wave field $G(f, \theta)$ to consist of a single wavenumber-direction component, that is, with a wavenumber magnitude k_0 and propagation direction θ, as shown in Fig. 2. Note that frequency ω and wavenumber k are related via the dispersion relation Eq. (3) and can be used interchangeably. For a side-scan pointing at an angle α_i (relative to the x axis), the contribution to the measured velocity will be reduced by a geometric factor $\cos(\alpha_i - \theta)$. More importantly, the side-scan will measure a different and smaller *apparent* wavenumber magnitude if it is not pointed parallel or antiparallel to the wave direction. The variation in apparent wavenumber magnitude is

$$k_a = k_0 \cos(\theta - \alpha_i). \quad (4)$$

Waves propagating nearly perpendicular to the beam will show a nearly zero apparent wavenumber magnitude (very long apparent wavelength).

Clearly the wavenumber and amplitude observed by a side-scan beam can be uniquely determined if the amplitude and direction of the surface waves are known. However, the reverse is not true and one cannot reconstruct the original wave spectrum from a single side-scan ping because an apparent wavenumber component could come from a wide range of *true* wave components, as indicated by the dashed lines in Fig. 2. Moreover, in a real ocean the wavenumber spectrum will be composed of contributions from an infinite number of wave field components. For any practical measurement problem, however, the continuous

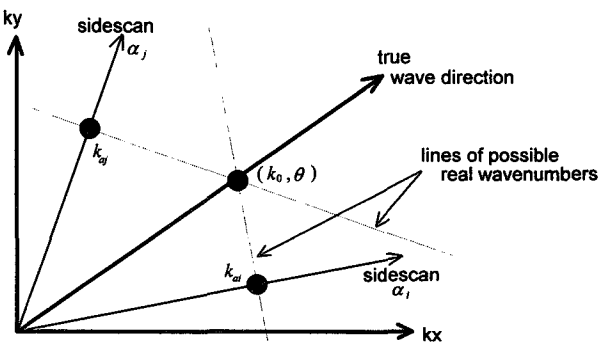

FIG. 2. Wavenumber diagram of a single wave component at (k_0, θ_0) sampled by two side-scan beams at angles α_i and α_j.

wavenumber spectrum must be discretized and reduced to a finite set of wave components. The fact that contributions from different wave field components are affected differently by changes in side-scan beam angle implies that one can *in principle* reconstruct the discrete wave spectrum from one (or more) side-scan sweeps. The problem at hand is to perform this reconstruction economically.

The procedure developed here uses CWS. A single sidescan ping measures horizontal water velocities at a series of equally spaced points on a line with direction α_i. Applying a Fourier transform, suitably windowed, gives us the apparent wavenumber spectral amplitudes $U(k_a)$ (complex) in the direction α_i. For each apparent wavenumber k_a, there is a range of real wave field components, given by Eq. (4), that could contribute to this component of $U(k_a)$. In wavenumber space these points all lie along a line perpendicular to α_i (see Fig. 2). The procedure then is to coherently increment all possible components by an amount proportional to the corresponding $U(k_a)$. A complex amplitude averaging array $A(f, \theta)$, having a polar grid in wavenumber space is used for this summation. The simple case in Fig. 2 shows how wave components from two sidescan pings will increment $A(k_0, \theta_0)$, the true wavenumber vector. In addition many other wavenumbers will be incremented where there is no true wave power. With temporal and spatial phase deconvolution (discussed below), all true increments to $A(k_0, \theta_0)$ will add up, while increments to other wavenumbers will not be deconvolved properly due to the dependence of the phase factors on k and θ. These spurious components will add incoherently, increasing as $(n^{1/2})$, while true wave components increase as n, the number of pings. The actual $D(f, \theta)$ is taken at the end of the summation as the squared magnitude of $A(f, \theta)$.

For the coherent summation, some convenient choice of wavenumber-directional grid must be predefined. In our implementation, the polar wavenumber grid for coherent summation uses 31 linearly spaced frequencies (or 31 wavenumber magnitudes) from 0.05 to 0.35 Hz and 120 directions (3° directional resolution). A great deal of flexibility is possible in choosing the start range and increment along the side-scan beam. In the *long* configuration, the fundamental wavenumber spectral amplitudes are derived from the spatial FFT of $N = 64$ velocity estimates starting at minimum range, $r_0 = 50$ m, and with a horizontal spacing, $\Delta r = 3.2$ m. This implies a wavenumber increment of 0.0307 m^{-1}. An alternate (short) configuration with $r_0 = 50$ m and $\Delta r = 2.0$ m is used also. To extract frequency components lower than 0.08 Hz the maximum side-scan range would have to be extended beyond 300 m. With the current equipment this is only a marginal prospect due to diminished signal-to-noise ratios at greater ranges. Before calculating the FFT, the range-averaged velocity along the beam is removed and a cosine-squared tapering window is applied. Application of the tapering window to the 64 velocity points has the beneficial effect of reducing the dependence on both short-range velocities, which are phase contaminated due to nonzero vertical grazing angles, and large ranges that suffer from low signal-to-noise ratios.

The coherent summation and interpolation scheme increments the entire $A(f, \theta)$ for each side-scan ping at direction α. At each grid point in $A(f, \theta)$ (i.e., for a particular k_0, θ), the corresponding apparent wavenumber magnitude is calculated using Eq. (4). Since this apparent wavenumber will not (in general) coincide with the FFT wavenumbers, the spectral amplitude increment is linearly interpolated within $U(k_a)$, taking care to use both positive and negative apparent wavenumber magnitudes. After coherently summing over a 64-ping sweep (38.4 s), a spreading function estimate $D(f, \theta)$ is calculated by taking the squared magnitude of $A(f, \theta)$ around each wavenumber magnitude (frequency). These 64-ping estimates are then incoherently averaged over roughly 40–50 min of data. Finally, the $D(f, \theta)$ are normalized at each frequency so that the integral over all directions is unity, as in Eq. (2). Increased sweep averaging improves the high-frequency stability and smoothness. However longer, statistically stationary datasets are not always available.

An angular weighting function is used so that wavenumber spectral amplitudes nearest to the side-scan beam direction are incremented more strongly. Because of the cosine weighting of velocity with direction, nearby wave directions contribute more heavily to $U(k_a)$ and thus have improved signal-to-noise properties. Also, wave components observed at large angular deviations have much lower apparent wavenumbers, where they are liable to be overshadowed by larger amplitude, true wave components at that direction. (Remember that typical wavenumber spectra fall off roughly as k^{-3}.) Thus, the weighting function was chosen to have the form

$$W(f, \theta) = \frac{|\cos(\theta - \alpha)|^p}{\omega}, \qquad (5)$$

where the exponent p is an adjustable parameter controlling the spread of wave power to nearby directions and frequencies. Powers of 10 or more reduce to less than 5% any components more than ±42° away from the side-scan beam direction, with the adverse effect of slight increase in angular spreading as p is increased. Values of p in the range 4–8 give good results, and $p = 5$ was used for the calculations presented here. The ω in the denominator of the weighting function converts velocity amplitude to wave height.

To ensure that coherent addition of successive pings occurs, temporal and spatial phase corrections must be applied. Because the side scan does not sample all directions simultaneously, the wave field will evolve during the side-scan sweep. Thus, each increment to $A(f, \theta)$ is multiplied by a time deconvolution factor

$\exp(-i\omega t)$, with t being the time of the ping relative to the start of the sweep. The frequency ω is that corresponding to the point $A(f, \theta)$ being incremented, not the apparent frequency of the $U(k_a)$ value that produced the increment. This time deconvolution enables successive pings of the sonar to be combined, the only limit being the decorrelation time of ocean waves.

The spatial phase correction arises as the sidescan beam rotates in the wave field. In this case the sidescan array extends outward from radius r_0 as it rotates about the origin (platform location), with the length of the array given by $N\Delta r$, the number of elements times the range increment. The origin of the spatial FFT is taken at the point (r_0, α). As the side-scan beam rotates, the array origin sees a different phase; that is,

$$\phi = kr_0 \cos(\alpha - \theta). \quad (6)$$

In this case k and θ are the wavenumber and direction of the wave being observed [i.e., the $A(f, \theta)$ being incremented]. Each increment to $A(f, \theta)$ is multiplied by this spatial deconvolution factor, that is, $\exp(-i\phi)$. The spatial phase correction allows one to combine data from several sonar beams operating simultaneously, provided they rotate about a common center.

As hinted earlier, there are natural and process-imposed limits to the spatial and temporal coherence of this CWS method. It is a reasonable hypothesis that a natural wave field will exhibit only limited spatial or temporal phase coherence, especially when the effects of changing wind conditions, "wave groupiness," and wave breaking are considered. For example, to explain nonlinear wind-wave behavior, Mollo-Christensen and Ramamonjiarisoa (1978) and Ramamonjiarisoa and Mollo-Christensen (1979) proposed models using Stokes-like wave groups with spatially and temporally localized amplitude and phase modulation. Also important are the effects of the finite spectral area represented by each wavenumber-directional component. The fundamental data source is the spatial FFT along each side-scan beam, which has a wavenumber resolution $\delta k = \pi/N\Delta r$. Considering two wave components separated by δk but falling within the same FFT bin, an estimate of the spatial coherence scale is $\pi/\delta k$, or the FFT aperture (in our case 128 or 205 m). The decorrelation time is then this array aperture divided by the wave group speed. For example, with the first FFT component at $k = 0.0307$ m^{-1}, the group speed is 8.9 m s^{-1}, yielding a decorrelation time of 23 s. Higher wavenumbers have longer decorrelation times (e.g., at $k = 0.307$ m^{-1}, the decorrelation time is 73 s). However, these timescales are typically short or comparable to the time required for one 360° side-scan sweep. This is the reason for coherently averaging over only one 64-ping sweep. Attempted longer coherent averaging results in negligible gain in directional resolution, as the true wave amplitudes begin to add incoherently in a similar fashion to the spurious wave components. Additionally, the amplitude weighting function [Eq. (5)] has the beneficial effect of reducing dependence on low-wavenumber components that have shorter decorrelation timescales.

An intimately related problem to temporal decorrelation is the coarse directional resolution provided at low frequencies. The temporal deconvolution is not able to select between two waves with roughly the same wavenumber magnitude (i.e., within the same FFT bin) but different directions. This leaves the spatial phase deconvolution to provide directional discrimination. To quantify the spatial phase resolution, consider a simple example of a single wave component with wavenumber k propagating at direction θ. If we incorrectly assume the wave is traveling toward angle $\theta + \delta\theta$ (perhaps due to a directional spread in the wave field), then the spatial phase error E is given by Eq. (6) as

$$E = kr_0[\cos(\theta - \alpha - \delta\theta) - \cos(\theta - \alpha)]. \quad (7)$$

As the side-scan looking angle α changes, the phase error will vary from zero at $\theta - \alpha = 0.5\delta\theta$ to a maximum when $\theta - \alpha = 0.5(\delta\theta + \pi)$, at which point the phase error becomes

$$E_{\max} = 2kr_0 \sin\left(\frac{1}{2}\delta\theta\right). \quad (8)$$

For effective phase discrimination to occur, $E_{\max}$ should change by at least 90° as the side-scan beam rotates, so we shall take $E_{\max} = \pi/4$ as a criterion for angular resolution. Then $2\delta\theta$ should approximate the minimum full width half maximum (FWHM) resolution of the method. The predicted FWHM limits will decrease with frequency, yielding at 0.09, 0.10, and 0.11 Hz limits of 56°, 45°, and 37°, respectively. This indicates that the best way to improve directional resolution is to increase r_0. This simple analysis neglects the effects of the finite wavenumber resolution within the spatial FFT and the fact that coherent increments to $A(f, \theta)$ are calculated via interpolation over a range of spatial FFT components. These resolution limits will be evaluated using synthetic data in the next section.

To quantify comparisons between directional spectra, bulk directional statistics can be used. The mean direction is commonly calculated as the phase angle of the first complex component (a_1, b_1) of the discrete Fourier transform of the directional distribution; that is,

$$\theta_{\text{mean}}(f) = \arctan\left(\frac{b_1}{a_1}\right). \quad (9)$$

Significant differences between the mean and peak (θ_{peak}) directions is an indication of wave field multimodality. Also, the directional spread is defined as the standard deviation of $D(f, \theta)$; that is,

$$\Delta\theta(f) = \left[\int_{\theta_{\text{mean}}-\pi}^{\theta_{\text{mean}}+\pi} (\theta - \theta_{\text{mean}})^2 D(f, \theta) d\theta\right]^{1/2}. \quad (10)$$

This directional spread parameter is quite sensitive to off-peak noise and alternate wave field modes. Another measure of the directional spread is the FWHM, which describes the width of the main peak, ignoring sidelobes.

Reference height and directional spreading functions will be needed in the next section to generate synthetic data and to compare with experimental results in section 5. A useful reference for the wave height spectrum is the well-known JONSWAP (Joint North Sea Wave Project) spectral form [Hasselmann et al. (1973), with constants for open Pacific Ocean taken from Chiswell and Kibblewhite (1981)]

$$S(\omega) = \alpha g^2 \omega^{-5} \exp\left[-1.25\left(\frac{\omega}{\omega_p}\right)^4\right]\gamma^b, \quad (11)$$

where ω_p is the peak spectral frequency, $\alpha = 0.0081$, $\gamma = 1.55$, $\sigma = 0.09$, and $b = \exp[-(\omega - \omega_p)^2/2\sigma^2\omega_p^2]$. Assuming an equilibrium wind-driven wave field (a limiting case requiring large fetches and steady wind for long duration), we can calculate the peak frequency from $f_p = g/2\pi u_{10}$, where u_{10} is the wind speed at 10-m height. For example, a 10 m s^{-1} wind would correspond to $f_p = 0.156$ Hz. Also, Donelan et al. (1985) and Banner (1990) recommend for an equilibrium wind sea a directional spreading functional form

$$D(\theta) = \frac{1}{2}\beta \cosh^{-2}[\beta(\theta - \theta_{\text{mean}})], \quad (12)$$

with the spreading coefficient β dependent on frequency as

$$\beta = \begin{cases} 2.61(\omega/\omega_p)^{1.3}, & 0.56 < \omega/\omega_p < 0.95 \\ 2.28(\omega/\omega_p)^{-1.3}, & 0.95 < \omega/\omega_p < 1.6 \\ 10^{-0.4+0.8393\exp[-1.134\ln(\omega/\omega_p)]}, & \omega/\omega_p > 1.6 \end{cases} . \quad (13)$$

4. Synthetic data tests

The purpose of these numerical simulations was to demonstrate and quantify the accuracy and resolution of this CWS method. It was thus necessary to numerically simulate wave fields of known directional and frequency spectra. The simulations assumed the wave field to be composed of a large number of independent Fourier components (in both frequency and direction) obeying linear dispersion. The basic formulation used a summation over M frequencies and N directions:

$$u_{\text{radial}}(x, y, t) = \sum_{i}^{M}\sum_{j}^{N} \omega_j \cos(\alpha - \theta_j)[S(f_i)D(f_i, \theta_j)]^{1/2} \times \cos(\omega_i t - k_{xi}x - k_{yi}y + \phi_{ij}). \quad (14)$$

The side-scan array locations (x, y) were calculated along the side-scan beam at azimuthal angle α. The wavenumber magnitudes were derived from the dispersion relation, with

$$k_{xi} = k(\omega_i)\cos\theta_j \quad \text{and} \quad k_{yi} = k(\omega_i)\sin\theta_j, \quad (15)$$

and with each wave component having an individual phase ϕ_{ij} randomized modulo 2π. Equations (12)–(14) with $u_{10} = 12$ m s^{-1} were used to calculate the directional spectrum. Note that this method produces a spatially and temporally coherent wave field obeying linear dispersion at all frequencies, which is not completely realistic. The individual wave component phases were randomized again after every 64-ping sweep (38.4 s) in an attempt to simulate the natural temporal decorrelation of ocean waves. Clearly the simulations will be improved by increasing the number of wave components, at the cost of increased calculation time. In these wave field simulations the directional spectrum was evaluated at 96 frequencies from 0.01 to 0.5 Hz and 360 directions in a full circle, which seemed a reasonable compromise. This resulted in 5–11 frequency components within each spatial FFT bin for each of the 360 wave field directions. The synthetic data were calculated at 0.6-s intervals for 80 × 64 ping sweeps, following the side-scan sweeping geometry as outlined above. A minimum of about 40 sweeps was required for sufficiently stable results. A random noise velocity of 0.2 m s^{-1} amplitude was added to the synthetic wave velocities to include the effects of Doppler estimation uncertainty mentioned in section 2.

We can quantify the minimum directional resolution and accuracy of this CWS method using a single-direction (plane) JONSWAP wave field, with results summarized in Table 1. In essence, this test generated the *directional impulse response* functions for this CWS

TABLE 1. Frequency variation of peak direction, mean direction, spread, and FWHM (all in degrees) of directional spreading functions for a plane wave ($\theta = 160°$) JONSWAP spectrum ($u_{10} = 12$ m s^{-1}) simulation. Predicted FWHM from Eq. (8) using $E_{\max} = 0.29\pi$.

Frequency (Hz)	θ_{peak} (°)	θ_{mean} (°)	$\Delta\theta$ (°)	FWHM (°)	Predicted FWHM (°)
0.09	135	157.9	53.4	75	64.9
0.10	162	161.4	41.5	51	52.3
0.11	156	159.3	29.6	39	43.1
0.12	159	160.2	22.4	33	36.2
0.14	159	159.9	35.9	24	26.5
0.16	162	161.3	44.2	21	20.3
0.18	159	159.3	52.4	15	16.0
0.20	159	160.7	63.2	12	13.0
0.22	159	159.9	63.4	9	10.7
0.24	159	159.5	71.8	9	9.0
0.26	159	159.3	70.6	9	7.7
0.28	159	158.5	81.4	9	6.6
0.30	159	159.2	83.0	9	5.8
0.32	159	157.1	87.6	6	5.1
0.34	159	154.9	92.6	6	4.5

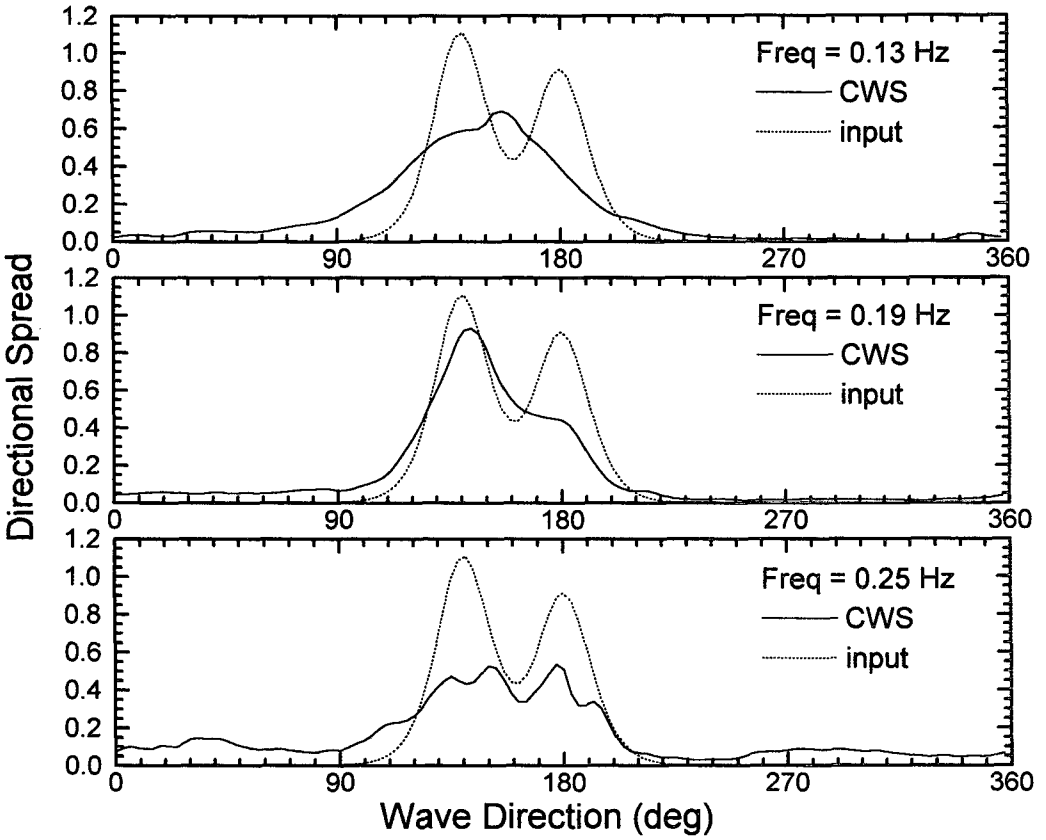

FIG. 3. Comparison of CWS and input directional spreading functions at 0.13, 0.19, and 0.25 Hz for bimodal wave simulation. Input spreading function has $\theta_{peak} = 140°$, peak separation of 40°, and uses a JONSWAP height spectrum with $u_{10} = 12$ m s^{-1}.

method. The peak direction was recovered to ±1.5° in the frequency range 0.1–0.35 Hz. The average over 0.1–0.34 Hz of θ_{mean} was 160° ± 2°. Note that with increasing frequency the directional resolution improved, as indicated by a decreasing FWHM but with an increasing directional spread. The minimum directional spread was 22° at 0.12 Hz. At the higher frequencies, the angular resolution (as measured with FWHM) approached the 6° numerical resolution of the directional grid. At all frequencies the peak power in the sidelobes was less than approximately 5% of the peak power. Clearly for very narrow wave fields the presence of small, incoherent, omnidirectional noise levels (which are a consequence of the coherent summation) adversely affected the directional spread.

At lower frequencies the angular resolution was fairly poor, for reasons discussed above. As shown in Table 1, the measured FWHM were in agreement with predicted values [using $E_{max} = 0.29\pi$ in Eq. (8)] derived from simple geometrical considerations. In particular, Eq. (8) has the correct functional form versus frequency. This suggests that it is the poor spatial phase discrimination, not the finite wavenumber resolution, that is the controlling parameter for directional resolution. These plane wave results were found to be quantitatively similar when choosing other wave directions; that is, no directional bias in this method was observed. This is perhaps a consequence of using a side-scan stepping scheme that covered all directions uniformly.

A more realistic test of the CWS method using a bimodal spread JONSWAP spectrum was performed, with results at three frequencies shown in Fig. 3. The input directional spread was a superposition of two spreading functions as in Eq. (12) with $\beta = 4$ and angular separation of 40°. In general, the main peak ($\theta_{peak} = 140°$) was extracted, with the average value across the frequency range 0.1–0.30 Hz of $\theta_{peak} = 142° \pm 5°$. In the 0.25-Hz curve (and at higher frequencies) the omnidirectional noise floor can approach 20% of the peak wave power, which is a consequence of the added random noise relative to the coherent wave signal. This noise floor does not go away with more sweep averaging, it just gets smoother and will adversely affect calculations of directional spread. At low frequencies (typically shown by the 0.13-Hz result) the method has insufficient resolving power to separate the two peaks. Improved results could be obtained by main-

taining the phase coherency and coherently summing for longer than a single 64-ping sweep.

The CWS algorithm is also fairly insensitive to incoherent noise. The simulations shown in Fig. 3 (and many others) yielded essentially identical results when performed without the 0.2 m s^{-1} added random velocity noise. To further test the noise immunity, a plane wave test (similar to Table 1) was repeated with larger levels of added random noise. Figure 4 shows a directional spreading result that approached the lower S/N limit of operation. In this case the added noise was 1.43 m s^{-1} (rms), or about 3.3 times the coherent wave velocity signal. The main peak can be readily identified from the noisy background up to 0.31 Hz. However, the minimum FWHM for this case was 15°. Clearly, the coherent summation technique used here is effective in reducing the effects of random, incoherent noise in the presence of a spatially coherent signal.

Finally, a numerical dataset consisting entirely of random velocity fluctuations without any coherent wave structure was generated. The directional spectrum calculation produced only omnidirectional background noise at all frequencies, with no consistent peaks or nulls in the directional spreading functions. This null directional result reinforces the conclusion that there exists no preferred direction or geometry within the method.

5. Analysis of ocean data

The SeaScan instrument platform was deployed as part of a larger acoustic study of ocean surface processes during a 3-week period in December 1993. To demonstrate the performance of this CWS method we shall focus on a 36-h deployment on 2 and 3 December (all times PST). The location was in the northeastern Pacific Ocean near 48.8°N, 127.0°W. The wind speed and direction (at 3-m height), air and water temperature, and barometric pressure were measured with a meteorological buoy (Minimet), which was freely drifting within 2 km of SeaScan. A plot of wind climate from Minimet for 2 and 3 December (year-days 336 and 337) is shown in Fig. 5. The winds were dominated by the passage of three frontal systems, with particularly rapid changes in wind speed and direction on year-days 336.6 and 337.4. This created multimodal wind-sea and swell wave fields. Due to the rapid (<12 h) changes in wind climate, the wind-sea components of the wave field were *duration* limited (i.e., not equilibrium spectra) and continually shifting in direction. In such cases the local wind could be only a rough predictor of wave fields that were generated distantly by these moving storms. Due to the continual presence of storm events and moderately strong winds at the SeaScan location, the significant wave height stayed near 4.0 m throughout the period 336.5–338.0. This multimodal, rapidly evolving wave climate makes interpretation of the directional spectral results more complicated, as it is difficult to separate measurement limitations from natural wave field properties.

First, we shall focus on an azimuthally scanning side-scan dataset taken at 1305–1356 PST 3 December (year-days 337.54–337.58). The average wind during

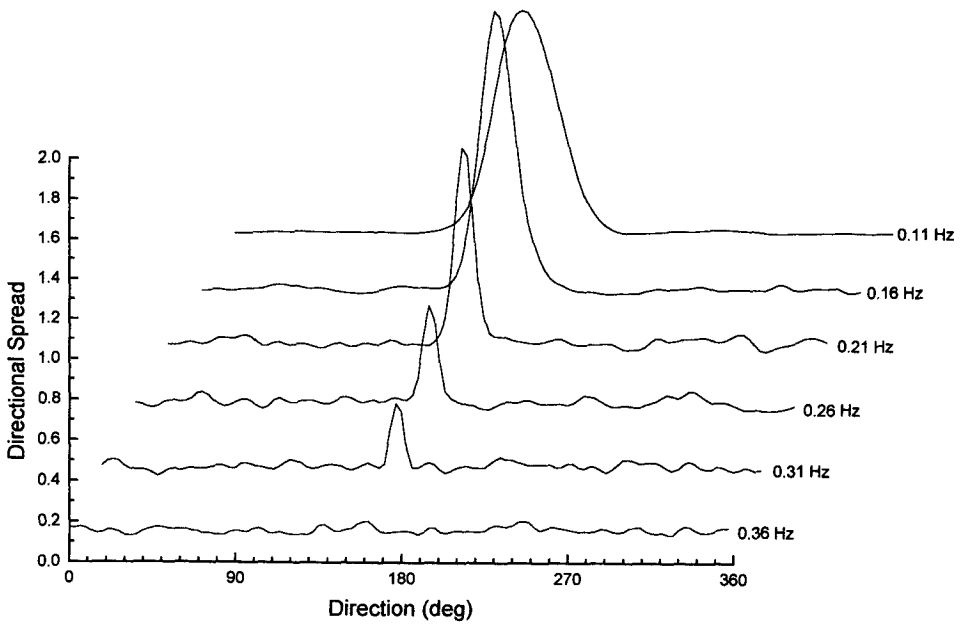

FIG. 4. Directional spreading results at six frequencies for synthetic plane-wave-plus-noise test. Input direction was 160° with 1.43 m s^{-1} rms, added random velocity noise. Each curve offset 0.3 vertically and 18° horizontally.

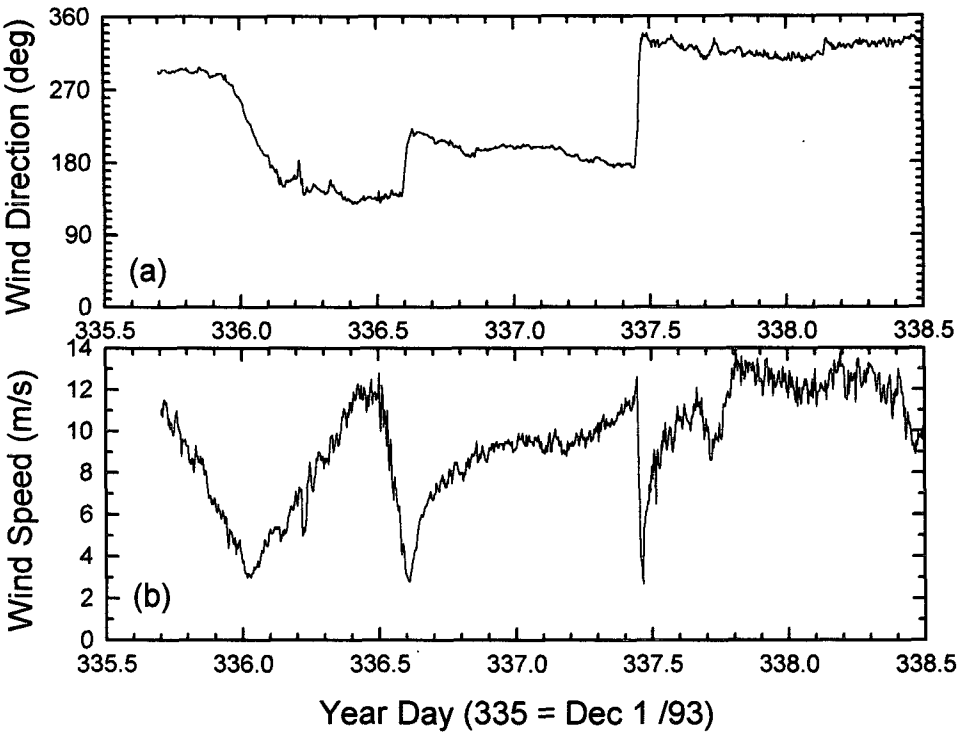

FIG. 5. Minimet wind (a) direction and (b) speed at 3-m height from the northeastern Pacific during year-days 335.5–338.5 (PST), 1993. Minimet buoy located near 48.8°N, 127.0°W.

this time was 10.8 m s^{-1} (corrected to 10-m height) from a direction 325° ± 5°T, with air and water temperature of 7.5° and 10.4°C, respectively. Note however, the abrupt change in wind direction about 2 h before this dataset, yielding a rapidly developing wind sea propagating toward 145° and a residual sea swell propagating toward 020° from the previous storm event. The instrument platform was suspended at a mean depth of 22.4 m.

Using standard FFT methods the surface wave height spectrum $S(f)$ can be calculated from the instantaneous surface elevation, as shown in Fig. 6. This spectrum was calculated from 50 point × 128 point FFT, yielding a frequency resolution of 0.013 Hz. For this spectrum the significant wave height was 4.00 m and the peak frequency was 0.085 Hz. The spectrum was dominated by *swell* components with frequency 0.05–0.11 Hz. A secondary peak (frequency 0.12–0.17 Hz) was also observed. With a 10.8 m s^{-1} wind speed, the equilibrium wind–wave *sea* should have a peak frequency near 0.144 Hz. However, the wind drastically veered at 1130 PST that day, so the wind sea was duration-limited with an observed peak near 0.20 Hz, corresponding to a wave age (c_p/u_{10}) of 0.66. The dotted lines show equilibrium JONSWAP wind-sea spectra for two wind speeds. Note that the peak at 0.14 Hz nearly matches the 12 m s^{-1} wind-sea reference, suggesting that this peak is a remnant of the south-southeast wind that existed only 4 h earlier. The measured and reference spectra are in agreement above 0.25 Hz, but several more hours wind-wave growth are needed to match the reference spectral peaks.

The range-averaged velocity along a side-scan beam can be used to calculate the surface drift current relative to the platform, as shown in Fig. 7a. This range-averaged velocity variation exhibited wavelike components (~±0.3 m s^{-1}) due to horizontal platform motion and averaging wave components longer than the 205-m aperture of the side-scan beam. The first circular harmonic has magnitude 0.12 m s^{-1} and direction 159°. Examination of the vertical accelerometer signal revealed that the platform was coupled to the wave orbital motion at 22.5-m depth induced by swell (~12-s period, demonstrated in T95). However, the circular harmonic decomposition separated this platform motion contamination, as revealed by the time history of magnitude and direction of surface current shown in Fig. 7b. The ensemble vector-averaged surface drift (relative to the platform) was 0.066 m s^{-1} toward 188°. From nearly hourly Argos positions of the surface buoy, the platform drifted with the 50-m-deep mixed layer at 0.48 m s^{-1} toward 141°, for a total surface drift current of 0.53 m s^{-1} toward 146°.

Approximately 51 min of side-scan horizontal velocity data along both rotating side-scan beams were collected and used in the CWS algorithm to estimate the directional spectrum as shown in Fig. 8. The contours are $\log10[G(f, \theta)$ re m^2 Hz^{-1} $rad^{-1}]$ in 0.2 in-

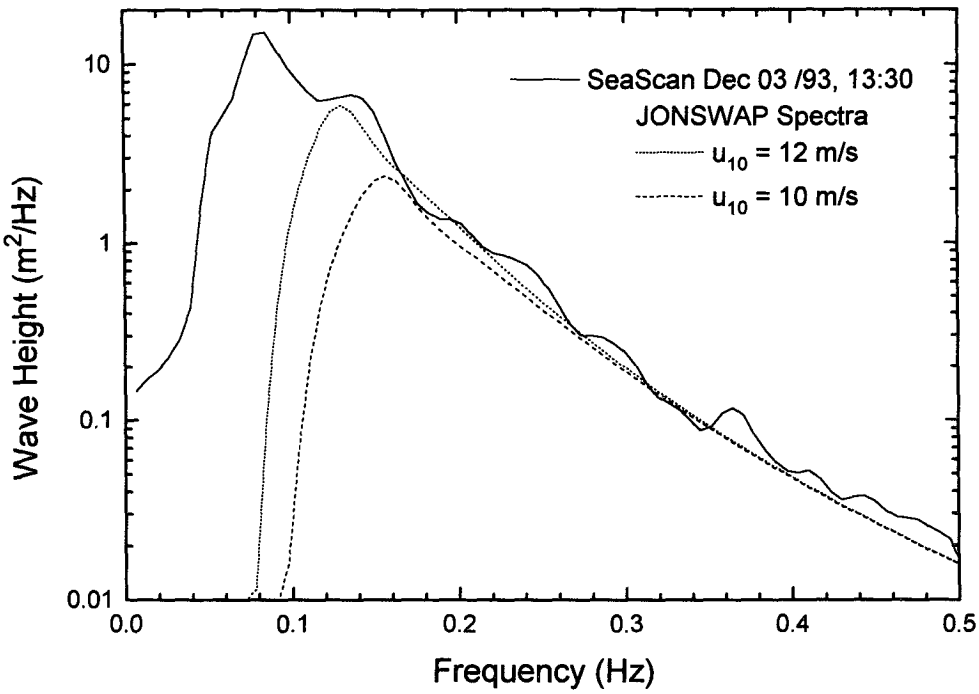

FIG. 6. Wave height vs frequency spectrum from SeaScan vertical sonars at 1330 PST 3 December 1993 in the northeastern Pacific Ocean. Spectrum is averaged over 50 × 128 samples at 0.6 s per sample. For comparison are plotted reference JONSWAP wind-sea spectra.

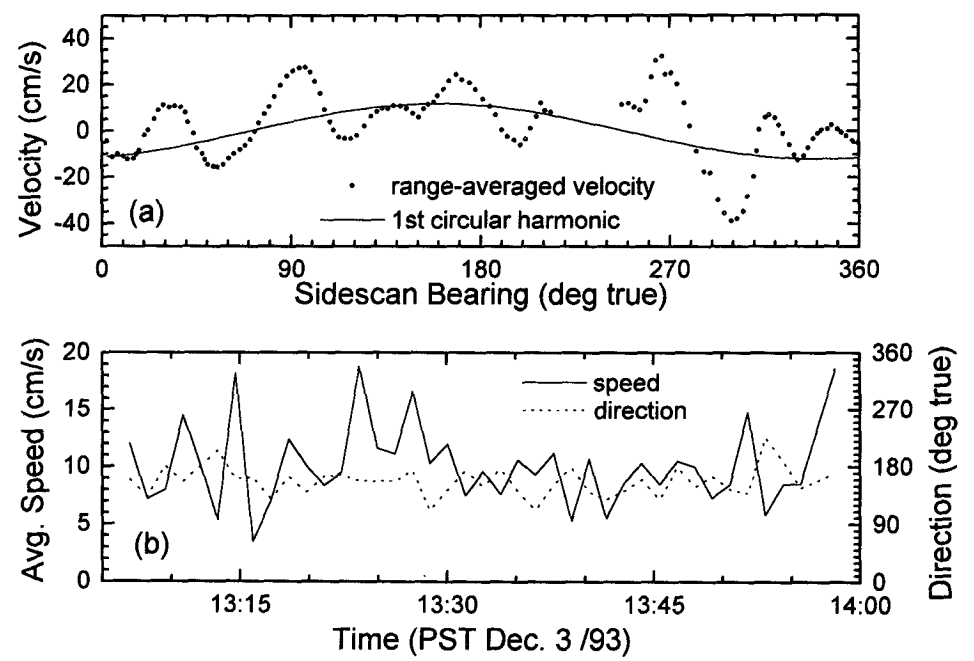

FIG. 7. Relative surface drift current extracted from range-averaged velocity: (a) azimuthal variation over 128 pings from one side scan at 1305 and (b) magnitude and direction over period 1305–1355 PST 3 December 1993.

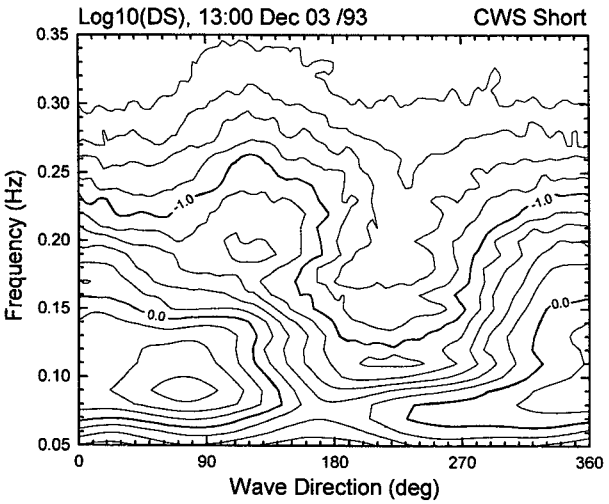

FIG. 8. CWS directional spectra using short-range configuration at 1300 PST 3 December 1993. Waves propagate toward direction shown. Contours are log10 with minimum −1.8 and increment 0.2.

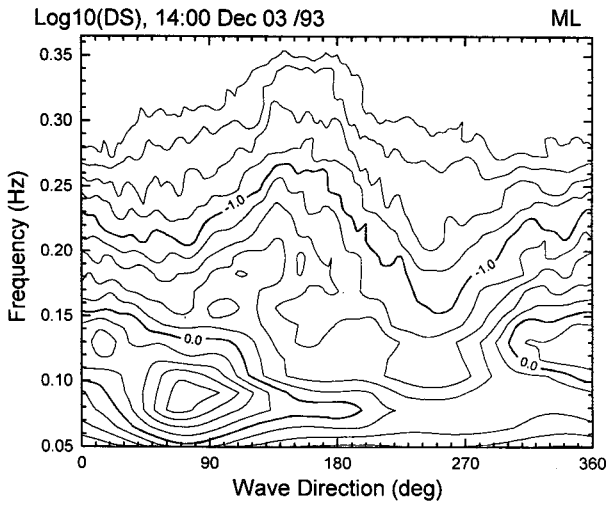

FIG. 9. Wave directional spectrum derived from maximum-likelihood analysis of side-scan array data at 1400 PST 3 December 1993 (contours as in Fig. 8).

crements. Figure 8 uses the short geometry with aperture from 50 to 152 m. A reference directional spectrum taken at 1400 to 1500 PST on this day, calculated using a maximum-likelihood (ML) algorithm as described in T95, is shown in Fig. 9. Both directional spectra clearly revealed separate propagation directions for the active wind sea (0.18–0.30 Hz, ~140°), a remnant wind sea (0.08–0.25 Hz, ~020°), and a long period swell (0.06–0.14 Hz, ~075°). The remnant wind sea was due to the south-southeast wind from yeardays 336.6–337.45. Note from both spectra the presence of higher-frequency (up to 0.25 Hz) wave energy from the remnant wind-sea group, resulting in a bimodal sea state between 0.18 and 0.25 Hz. Also, the ML active wind-sea spectrum shows a clear southerly shift in peak direction by 10°–15° with increasing frequency, probably due to the higher frequencies responding more rapidly to the local wind direction.

Methods for partitioning such multimodal directional spectra into individual wave groups were discussed in Gerling (1992), from which we draw the concept of partial significant wave height (PSWH), defined as

$$\mathrm{PSWH} = 4\left[\int_{f_1}^{f_2}\int_{\theta_1}^{\theta_2} G(f,\theta)\,d\theta\,df\right]^{0.5}. \quad (16)$$

The frequency and directional limits were chosen through examination of the spectral contour plots and the directional analyses [Eqs. (9) and (10)]. For example, the directional limits were taken as ±50° from the peak direction [in Gerling's case the process was automated and integrated over curved regions in $G(f, \theta)$]. The mean and peak directions, directional spread, and FWHM for the wave group were averaged over the selected frequency interval. Thus, we can identify wave groups by peak frequency and direction, and the PSWH quantifies the strength of each. Directional parameters from Figs. 8 and 9 are compared in Table 2. In general the CWS results agreed with the ML statistics, except for several aspects. For the active wind sea, the CWS result showed peak and mean propagation directions shifted easterly by approximately 15° relative to the ML result. This may be partially accounted for by the wind-wave growth at higher frequencies between 1300 and 1400 PST. As already discussed, the CWS directional resolution was limited at low frequencies (<0.12 Hz), resulting in much larger FWHM for the swell group. Additionally, for the active wind sea the

TABLE 2. Comparison of bulk directional statistics from CWS (Fig. 8) and ML (Fig. 9) directional spectra.

Wave component	CWS	ML
Swell (0.06–0.13 Hz, 30°–130°)		
f_{peak} (Hz)	0.09	0.091
θ_{peak} (°)	075	078
FWHM (°)	108	61
PSWH (m)	2.15	2.36
Remnant wind sea (0.11–0.25 Hz, 350°–070°)		
f_{peak} (Hz)	0.14	0.13
θ_{peak} (°)	023	018
FWHM (°)	64	50
PSWH (m)	1.35	1.22
Active wind sea (0.18–0.30 Hz, 080°–180°)		
f_{peak} (Hz)	0.20	0.182
θ_{peak} (°)	125	140
θ_{mean} (°)	131	144
$\Delta\theta$ (°)	94	86
FWHM (°)	107	72
PSWH (m)	0.82	0.91

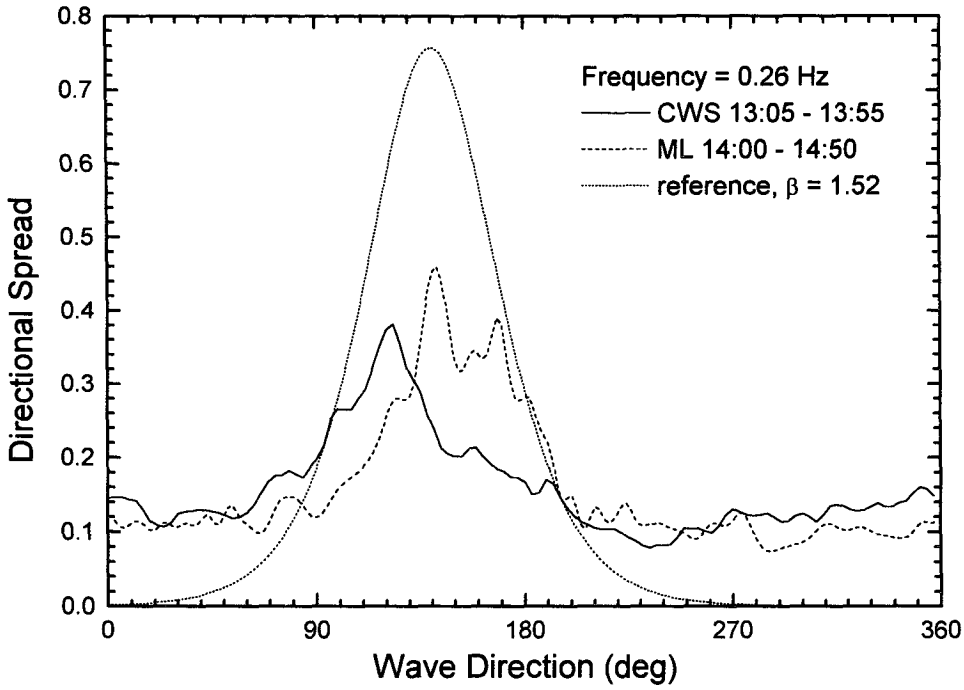

FIG. 10. Comparison of CWS short, maximum-likelihood, and reference (Donelan et al. 1985) directional spreading functions for wind-sea waves at 0.26 Hz.

CWS spread and FWHM were distinctly larger, perhaps due partially to the low wave age of the wind sea during this CWS data period.

Neither the CWS or ML methods was able to resolve properly the directional spread of the wind sea, as shown in Fig. 10. The reference curve is taken from Eqs. (12) and (13) using $\theta_{mean} = 140°$ and $f_{peak} = 0.20$ Hz, which thus predicts reference $\Delta\theta = 33.7°$ and FWHM = 69°. The shift in wave energy toward the south as the wave field strengthened is clear. In both cases the $\Delta\theta$ are considerably larger than the reference, although the FWHM of the ML result agrees well with the reference. The discrepancy could be partly due to the presence of higher-frequency wave energy from the remnant wind-sea group and the duration-limited nature of the wind sea.

Through partitioning all the CWS and ML directional spectra available during this 36-h deployment, we can follow the evolution of four distinct wave groups and compare the wave group parameters of the two methods, as shown in Fig. 11. Overall there was agreement in peak frequency, direction, and PSWH between the CWS and ML results. In particular, note the increase in PSWH and decreasing peak frequency of the wind-driven seas during year-days 336.8–337.5 and starting with the new wind direction at year-day 337.5. A long period, westerly swell was present at 0.07–0.09 Hz throughout the deployment.

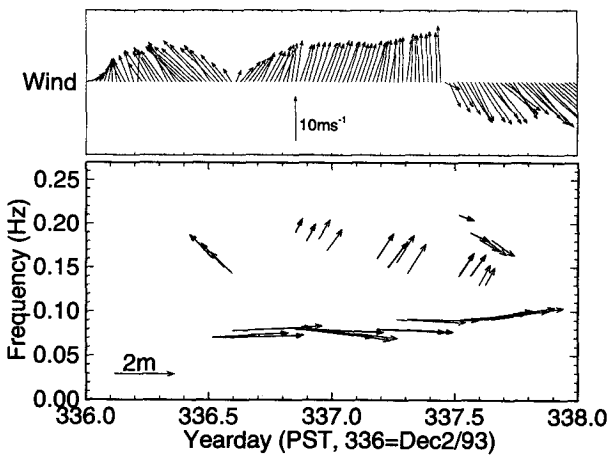

FIG. 11. Time evolution of f_{peak}, θ_{peak}, and PSWH comparing partitioned CWS (bold arrows) and maximum-likelihood directional spectra for 2 and 3 December 1993. North is toward the top of page.

6. Summary discussions

For the case of using one or more Doppler side scans in a full-circle sweeping mode, a new method has been developed to extract the directional spectrum of surface gravity waves. These directional wave results are intended to supplement the useful two-dimensional imaging capability provided by the rotating side-scans. Under typical oceanic conditions, breaking waves create a near-surface layer of microbubbles that act as

tracers of wave-induced fluid motion. Because of the continually varying side-scan looking angle, the entire frequency–directional spectrum must be solved simultaneously, and a coherent wavenumber summation technique is proposed. Wavenumber spectra along each side-scan beam measure the apparent wavenumber amplitudes, which are then used to increment all possible true wavenumber components. Temporal and spatial phase correction factors must be applied to ensure coherent summation. After coherently summing the spectral amplitudes over one 360° sweep, the true wave field components emerge and noise cancels out. Finally, the directional spreading functions from each sweep are incoherently averaged. The results improve with continued averaging, with a *minimum* of approximately 30 min (over 3000 separate pings) of data required.

Several factors limit the performance of this scheme. At frequencies above 0.3 Hz the rapidly diminishing wave velocities become lost in the natural bubble cloud variability and side-scan estimation noise, especially at longer ranges. At frequencies below 0.10 Hz the side-scan array dimensions provide insufficient spatial phase discrimination, resulting in an increased minimum directional spread or FWHM. Also, the side-scan array aperture (<205 m) imposes finite FFT wavenumber resolution and further imposes temporal coherence scales that are short or comparable to the time required for a 360° sidescan sweep (38.4 s). Interestingly, this geometry-imposed coherence timescale increases at higher frequencies. Increased coherent summation beyond these coherence times results in negligible performance improvements. Another problem would be departures from linear dispersive behavior. Both laboratory and oceanic evidence suggests that for active wind seas the wave celerity exceeds linear predictions (i.e., the wavenumbers are smaller, see Ramamonjiarisoa and Mollo-Christensen 1979). Since the CWS algorithm is particularly sensitive to wavenumber, such deviations might be significant. Further work in this area is needed.

Tests using synthetic data suggest that the CWS method has potentially good directional accuracy and resolution. Using unidirectional wave fields, the CWS method recovered the peak and mean directions to within ±2°. The typical directional spread for this plane wave test (as determined by the FWHM) decreased with frequency from 51° at 0.10 Hz to 6° at 0.35 Hz. However, the higher frequencies showed a somewhat larger omnidirectional noise floor, which (for example) approached 5% of the peak wave power at 0.35 Hz. The low-frequency performance was limited by the poor spatial phase discrimination of the side-scan aperture relative to the increasing wavelength. The low-frequency performance could be improved only by extending the maximum range of Doppler velocity estimation beyond 250 m. Additionally, this method was able to recover uni- and bimodal spread wave fields with adequate resolution and noise-rejection properties. The CWS algorithm was found to be immune to realistic ($\sim$0.2 m s^{-1}) random velocity noise levels within the target frequency range 0.08–0.30 Hz. The CWS method was able to extract coherent wave spectra down to signal-to-noise levels of 0.3. Furthermore, when using velocity data that uniformly covered all directions, this algorithm did not appear to have any inherent geometrical bias or preferred direction.

In a marked contrast to the excellent high-frequency performance predicted from numerical simulations, when applied to real ocean data the CWS method performed poorly at frequencies above 0.25 Hz. The CWS method was able to recover some integrated directional properties of the wave field, such as f_{peak}, θ_{peak}, and PSWH but had poorer directional resolution than the ML array method and reference wind-sea predictions. This is hypothesized as due to two factors: (i) deviations from linear dispersion and (ii) a decrease in the natural spatial and temporal coherence scales at higher frequencies, caused by wave breaking and wave *group* behavior. Note that the optimistic numerical results were derived from linear dispersive, phase coherent wave field simulations. In particular, for ocean data the directional spread and FWHM of the CWS results were much larger than predictions from literature. [Donelan et al. 1985, Eqs. (12), (13)] (Note that the ML array results were only minimally better.) However, all of the wave spectra (both ML and CWS) collected during this 36-h SeaScan deployment were duration limited and multimodal, which complicated directional spread comparisons. The unfortunate conclusion, however, is that the CWS method can extract only reliable mean direction, peak frequency, and integrated wave energy information.

Improved high-frequency performance might be achieved by using a velocity measurement technique with greater maximum range, faster ping cycle and azimuthal scan rate, and higher accuracy. A surface-grazing Doppler radar might meet these requirements. For side-scan systems, some small improvement in range and accuracy is technically feasible, but long-range scanning with a single beam requires a slower ping rate (e.g., to reach 500 m requires a travel time of 0.67 s). Multiple side-scan beams are a solution (albeit expensive) to this impasse.

Finally, azimuthal variations of the range-averaged, radial velocity can be processed to deliver estimates of the surface drift current relative to the instrument. The first circular harmonic was used to extract the surface drift current, which was then vector averaged over successive 360° sweeps in time. This method was effective at separating mean currents from low-frequency ($\sim$0.08 Hz) velocity contamination due to platform orbital motions.

Acknowledgments. The authors are indebted to Dr. David Farmer for the opportunity and encouragement

to pursue this work. The instrumentation and experimental developments were funded by grants from the Office of Naval Research. Support for the authors was also derived from the Canadian Interdepartmental Panel on Energy Resource Development. The suggestions and discussions of Dr. A. D. Booth were also appreciated.

REFERENCES

Banner, M., 1990: Equilibrium spectra of wind waves. *J. Phys. Oceanogr.*, **20,** 966–984.

Brumley, B., R. Cabrera, K. Deines, and E. Terray, 1991: Performance of a broad-band acoustic Doppler current profiler. *IEEE J. Oceanic Eng.*, **16**(4), 402–407.

Chiswell, S., and A. Kibblewhite, 1981: Spectra of the fully developed wind-generated ocean wave field west of central New Zealand. *N. Z. J. Mar. Freshwater Res.*, **15**(1), 81–84.

Crawford, G., and D. M. Farmer, 1987: On the spatial distribution of ocean bubbles. *J. Geophys. Res.*, **92**(C8), 8231–8243.

Donelan, M., J. Hamilton, and W. Hui, 1985: Directional spectra of wind-generated waves. *Philos. Trans. Roy. Soc. London, A,* **315,** 509–562.

Farmer, D. M., and S. Vagle, 1989: Waveguide propagation of ambient sound in the ocean-surface bubble layer. *J. Acoust. Soc. Amer.*, **86**(5), 1897–1908.

Gerling, T. H., 1992: Partitioning sequences and arrays of directional ocean wave spectra into component wave systems. *J. Atmos. Oceanic Technol.*, **9,** 444–458.

Hasselmann, K., and Coauthors, 1973: Measurements of wind-wave growth and swell decay during the Joint North Sea Wave Project (JONSWAP). *Dtsch. Hydrogr. Z.*, **A8**(12)(Suppl.), 95 pp.

Herbers, T., R. Lowe, and R. Guza, 1991: Field verification of acoustic Doppler surface gravity wave measurements. *J. Geophys. Res.*, **96**(C9), 17 023–17 035.

Krogstad, H., R. Gordon, and M. Miller, 1988: High-resolution directional wave spectra from horizontally mounted acoustic Doppler current meters. *J. Atmos. Oceanic Technol.*, **5,** 340–352.

Moll-Christensen, E., and A. Ramamonjiarisoa, 1978: Modeling the presence of wave groups in a random wave field. *J. Geophys. Res.*, **83**(C8), 4117–4122.

Pinkel, R., and J. Smith, 1987: Open ocean surface wave measurement using Doppler sonar. *J. Geophys. Res.*, **92**(C12), 12 967–12 973.

——, and ——, 1992: Repeat sequence coding for improved precision of Doppler sonar and sodars. *J. Atmos. Oceanic Technol.*, **9,** 149–163.

Ramamonjiarisoa, A., and E. Mollo-Christensen, 1979: Modulation characteristics of sea surface waves. *J. Geophys. Res.*, **84**(C12), 7769–7775.

Smith, J., 1989: Doppler sonar and surface waves: Range and resolution. *J. Atmos. Oceanic Technol.*, **6,** 680–696.

Trevorrow, M. V., 1995: Measurement of ocean wave directional spectra using Doppler side-scan sonar arrays. *J. Atmos. Oceanic Technol.*, **12,** 603–616.

——, and D. M. Farmer, 1992: A note on the use of Barker codes in Doppler sonar measurements. *J. Atmos. Oceanic Technol.*, **9,** 699–704.

——, and R. Teichrob, 1994: Self-contained acoustics platforms for probing ocean surface processes. *IEEE J. Oceanic Eng.*, **19**(3), 483–492.

——, S. Vagle, and D. Farmer, 1994: Acoustical measurements of microbubbles within ship wakes. *J. Acoust. Soc. Amer.*, **95**(4), 1922–1930.

Zedel, L., 1994: Deep ocean wave measurements using a vertically oriented sonar. *J. Atmos. Oceanic Technol.*, **11,** 182–191.